JOURNAL OF GEOPHYSICAL RESEARCH, VOL. 108, NO. A3, 1136, doi:10.1029/2002JA009707, 2003

Correction published 22 October 2003

Tail plasma sheet models derived from Geotail particle data

N. A. Tsyganenko

Universities Space Research Association and Laboratory for Extraterrestrial Physics, NASA Goddard Space Flight Center, Greenbelt, Maryland, USA

T. Mukai

Institute of Space and Astronautical Science, Sagamihara, Japan

Received 27 September 2002; revised 2 December 2002; accepted 9 January 2003; published 28 March 2003.

[1] Simple analytical models have been derived for the first time, describing the 2-D distribution (along and across the Earth's magnetotail) of the central plasma sheet (CPS) ion temperature, density, and pressure, as functions of the incoming solar wind and interplanetary magnetic field (IMF) parameters, at distances between 10 and 50 R_E. The models are based on a large set of data of the Low-Energy Particle (LEP) and Magnetic Field (MGF) instruments, taken by Geotail spacecraft between 1994 and 1998, comprising 7234 1-min average values of the CPS temperature and density. Concurrent solar wind and IMF data were provided by the Wind and IMP 8 spacecraft. The accuracy of the models was gauged by the correlation coefficient (c.c.) R between the observed and predicted values of a parameter. The CPS ion density N is controlled mostly by the solar wind proton density and by the northward component of the IMF. Being the least stable characteristic of the CPS, it yielded the lowest c.c. $R_N = 0.57$. The CPS temperature T, controlled mainly by the solar wind speed V and the IMF B_z, gave a higher c.c. $R_T = 0.71$. The CPS ion pressure P was best controlled by the solar wind ram pressure P_{sw} and by an IMF-related parameter $F = B_\perp\sqrt{\sin(\theta/2)}$, where $B_\perp$ is the perpendicular component of the IMF and θ is its clock angle. In a striking contrast with N and T, the model pressure P revealed a very high c.c. with the data, $R_P = 0.95$, an apparent consequence of the force balance between the CPS and the tail lobe magnetic field. No significant dawn-dusk asymmetry of the CPS was found beyond the distance 10 R_E, in line with the observed symmetry of the tail lobe magnetic field. The plasma density N is lowest at midnight and increases toward the tail's flanks. Larger (smaller) solar wind ion densities and northward (southward) IMF B_z result in larger (smaller) N in the CPS. In contrast to the density N, the temperature T peaks at the midnight meridian and falls off toward the dawn/dusk flanks. Faster (slower) solar wind flow and southward (northward) IMF B_z result in a hotter (cooler) CPS. The CPS ion pressure P is essentially a function of only X_{GSM} in the midtail (20–50 R_E); at closer distances the isobars gradually bend to approximately follow the contours of constant geomagnetic field strength. For northward IMF conditions combined with a slow solar wind, the isobars remain quasi-circular up to larger distances, reflecting a weaker tail current and, hence, more dipole-like magnetic field. *INDEX TERMS:* 2764 Magnetospheric Physics: Plasma sheet; 2744 Magnetospheric Physics: Magnetotail; 2784 Magnetospheric Physics: Solar wind/magnetosphere interactions; 2740 Magnetospheric Physics: Magnetospheric configuration and dynamics; 2753 Magnetospheric Physics: Numerical modeling; *KEYWORDS:* plasma sheet, solar wind, modeling, ion pressure, density, temperature

Citation: Tsyganenko, N. A., and T. Mukai, Tail plasma sheet models derived from Geotail particle data, *J. Geophys. Res.*, *108*(A3), 1136, doi:10.1029/2002JA009707, 2003.

1. Introduction

[2] The magnetotail plasma sheet (PS) is the most dynamic component of the magnetosphere, and probably the most important link in the Sun-Earth connection chain. It is a source of energetic particles for the inner magnetosphere and for the auroral precipitation. The cross-tail current flowing in the PS from dawn to dusk is a major part of the global magnetospheric current system, whose dynamics are controlled by the state of the incoming solar wind. The configuration of the nightside magnetospheric magnetic field is closely related to the particle pressure in the PS, owing to the approximate force balance under quasi-stationary conditions.

[3] Predicting changes in the PS spatial structure and dynamics in response to varying interplanetary conditions is a major challenge in understanding the space weather. Existing spacecraft data on the characteristics of PS par-

Copyright 2003 by the American Geophysical Union.
0148-0227/03/2002JA009707

ticles can be an abundant source of valuable supplementary information to space magnetometer data, helping test and refine the geomagnetic field models [*Tsyganenko*, 1990].

[4] The average large-scale distribution of the PS parameters has been studied using in-situ measurements in the PS [e.g., *Spence et al.*, 1989; *Kistler et al.*, 1993; *Hori et al.*, 2000; *Kaufmann et al.*, 2001], from low-altitude data combined with a model mapping [*Wing and Newell*, 1998, hereafter WN98; 2002], and from a particle simulation, using Geotail data as boundary conditions [*Wang et al.*, 2001]. All PS studies based on in-situ observations were confined either to the radial variation of the plasma parameters along the tail axis, or to their dawn-dusk profile. The first effort to overcome that limitation was made by WN98, who derived 2-D maps of the central PS (CPS) parameters. Their method was based on data of low-altitude polar satellites, combined with a mapping of the plasma parameters from the observation site into the distant magnetotail, using an empirical magnetic field model with adjusted parameters. That approach offered a promising tool for nearly real-time monitoring of the inner PS, but left uncertain the accuracy of the magnetic mapping at larger distances (beyond $\sim$15 R_E), where the stretch of the tail field lines is very sensitive to even small variations of the cross-tail current. Another limitation of previous work was that no attempt was made to correlate the global distribution of the CPS parameters to the concurrent state of the interplanetary medium at ordinary times, although several authors [e.g., *Baumjohann et al.*, 1989; *Kistler et al.*, 1993; *Huang and Frank*, 1994] did investigate the PS dynamics in the course of a substorm.

[5] This work continues the above studies and derives simple analytical approximations for the spatial distribution of the ion density, temperature, and pressure in the nightside part of the CPS, in the range of distances $10 < R < 50$ R_E. The models presented here describe the variation of the CPS parameters in two dimensions (along the Sun-Earth line and in the dawn-dusk direction) and include their dependence on the parameters of the solar wind found to be most effective. The study is based on a large set of in-situ data of Geotail's Low-Energy-Plasma (LEP) and magnetic field (MGF) instruments, taken from 1994 to 1998, as well as the concurrent solar wind and IMF data of IMP 8 and Wind spacecraft.

2. Data

[6] The primary source of data for this study was the DARTS online facility at the Institute of Space and Astronautical Science, Japan. PS parameters were obtained from the 12-s average plasma moments data, subsequently averaged over 1-min intervals and merged with concurrent magnetic field data, used in the identification of the CPS crossings. The data cover the 3.5-year period from November 1994 to April 1998; most of them correspond to the near-tail phase of the Geotail operation at distances between 10 and 30 R_E. Owing to the low inclination of the Geotail orbit, the data are concentrated either inside the PS or in the adjacent low-latitude tail lobes. More details on the Geotail orbit and its plasma (LEP) and magnetometer experiments can be found elsewhere [*Nishida*, 1994; *Mukai et al.*, 1994; *Kokubun et al.*, 1994].

[7] First of all, a crude elimination of the magnetosheath and solar wind data was made, based on the location of Geotail with respect to a model magnetopause, corresponding to a low value of the solar wind pressure of P_{sw} = 1 nPa and rotated around Z_{GSE} axis by 4 degrees, to take into account the aberration of the magnetotail due to Earth's orbital motion. All data points that fell outside that boundary were left out.

[8] The next step was to select crossings of the CPS by the spacecraft. Our crossing criterion was based on the observed radial component of the magnetic field

$$B_\rho = B_x \cos\phi + B_y \sin\phi, \tag{1}$$

where B_x and B_y are the components lying in the GSM equatorial plane and ϕ is the GSM longitude angle. A crossing was flagged when two consecutive 1-min average values of B_ρ had opposite signs, indicating a traversal of a sheet with mostly azimuthal direction of the current, and the corresponding plasma parameters were calculated as the average of the values just before and after the crossing.

[9] At an early stage of this study, a stricter criterion was also tried, requiring that three consecutive values of B_ρ were positive (negative) and three following ones were negative (positive), in other words, B_ρ was required to have the same orientation for 3 minutes before and 3 minutes after its reversal. The idea was to exclude small-scale local fluctuations of the turbulent magnetic field, retaining only clear-cut reversals of B_ρ, indicative of the spacecraft traversing a current sheet with a regular structure. However, the stricter criterion resulted in a severe reduction (by a factor $\sim$3) of the number of data records in the crossing set. For that reason, it was eventually decided to include all cases of B_ρ reversal. Both methods provided nearly the same spatial distribution of the crossings, which made us confident that in both cases most of the data belonged to the CPS. As detailed below, additional measures were also taken, to reject data from other adjacent plasma regions and exclude observations made during fast flow events.

[10] All crossings thus defined were collected into a single file and merged with concurrent solar wind data. Every data record was complemented by corresponding values of the solar wind density, speed, thermal speed, and IMF components, averaged over a 30-min interval immediately preceding the CPS crossing by Geotail. Owing to the good coverage of the period 1994–1998 by the data of Wind, only $\sim$25% of the Geotail data was left out by the lack of concurrent solar wind information.

[11] After that, the crossing data were filtered and a relatively small number of data records from the magnetosheath was removed. Such records existed because the initial data selection used an undercompressed (P_{sw} = 1 nPa) extra-large model magnetopause. A direct visual inspection and manual editing of the data was next attempted, using the observed values of the plasma flow speed, temperature, and density, but it was soon realized that an objective automated procedure was needed, based on a physically clear rejection/acceptance rule. A simple and effective plasma region indicator was found, using the ratio $\gamma = T/N$ between the ion temperature and their density. Cool and dense magnetosheath and low-latitude boundary layer (LLBL) plasmas have much smaller values of the

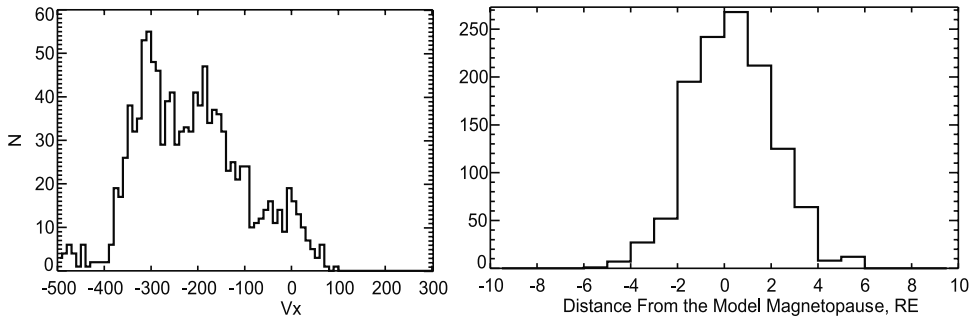

Figure 1. Distributions of the V_x component of the plasma flow velocity in the set of data rejected by the $\gamma < 5$ criterion (left), and of the distance to the model magnetopause, for the same data set (right).

parameter γ. Since those regions are usually associated with rapid and predominantly tailward flows, one might expect that most data records with low values of γ should also have large and negative values of the V_x component of the plasma flow velocity. This conjecture was fully confirmed by inspecting the rejected records.

[12] The adopted procedure selected all data records with $\gamma \geq \gamma_c$ and placed them in an active set, while the rejected data with $\gamma < \gamma_c$ were collected separately. This study used the rejection threshold $\gamma_c = 5$ kev·cm^3, and rejected 1213 records out of a total of 10431 records, flagged as possible CPS data. The adopted rejection criterion could also help filter out rare cases of the data contamination by bursts of high-energy electrons, observed during strong substorm acceleration events and resulting in unusually low (high) apparent temperatures (densities). However, the number of such events in our data set (if any) was vanishingly small: as shown below, almost all of the rejected data records were indeed associated with the LLBL.

[13] Figure 1 shows two histograms; the first (left) is a distribution of V_x in the rejected data, and the second (right) shows the distribution of the distance of the rejected data points from the model magnetopause [*Shue et al.*, 1998], calculated using the actual solar wind conditions for each data record. As clearly seen from the first histogram, most of the rejected data had large negative V_x, and only a small fraction had $V_x > 0$. As demonstrated by the second histogram, all these events were concentrated in a narrow layer around the model magnetopause, most of them within $\sim$3 R_E from the boundary. Very few data points lie more than 4 R_E outside it, owing to the initial crude pre-filtering, using the relaxed model boundary with $P_{sw} = 1$ nPa.

[14] The accepted data set was further reduced by removing all the data with sunward or tailward plasma flow speeds exceeding 150 km/s, in order to (1) limit the database to mostly quasi-static conditions, excluding major dynamic events such as substorms, plasmoids, fast reconnection, etc., and (2) eliminate data records pertaining to the boundary layer PS, where fast field-aligned flows are a common feature.

[15] The final crossing data set comprised 7234 records. Their spatial distribution projected on the GSM XY and YZ planes is shown in Figure 2. Most of the crossings correspond to the near-tail phase of the Geotail experiment (after 1994), at radial distances between 10 and 30 R_E. The more distant crossings between 30 and 50 R_E occurred in 1994 and in the beginning of 1995. As can be seen in the Figure 2b, most of the crossings in the dawn sector were observed southward from the GSM equatorial plane. This is due to the fact that most of the Geotail orbits passed through the dawn sector in winter, when the Earth's dipole tilt angle is negative and hence the plasma sheet is shifted southward from its average position. To quantitatively check the dipole tilt effect in the ordering of the crossings, we calculated and plotted in Figure 3 a distribution similar to that in Figure 2b, but with $\Delta Z = Z_{GSM} - Z_N$ instead of Z_{GSM} along the

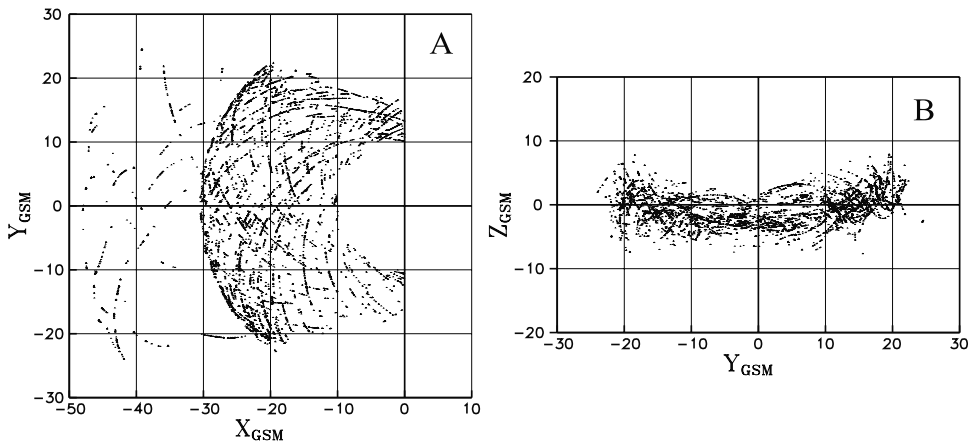

Figure 2. Distribution of the CPS crossings in the modeling data set: (a) projected on the equatorial (GSM XY) plane, and (b) in the cross-tail (GSM YZ) plane.

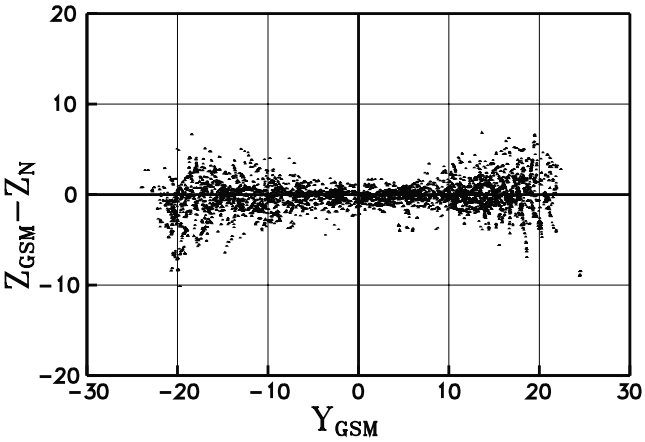

Figure 3. Distribution of the CPS crossings in the modeling data set, similar to those in Figure 2b, but with respect to a tilt-dependent warped current sheet with $Z_N = Z_N(X, Y, \Psi)$.

vertical axis. Here Z_N is the expected position of the center of the cross-tail current sheet, derived from our earlier study of the magnetotail geometry *Tsyganenko et al.* [1998], based on Geotail magnetic field data.

[16] As can be seen from the plot, the reduced positions of the crossings form an orderly symmetric cloud, closely grouped around the horizontal axis in the middle, but more dispersed near the tail flanks, where the plasma sheet becomes more unstable and turbulent. An additional check of the final data set was also made, based on the fact that the plasma beta parameter inside the CPS should be relatively high. Figure 4 shows a histogram of $\beta = 2\mu_0 P/B^2$ for the entire crossing data set. It is clearly seen that virtually all the crossings have $\beta > 1$, while in 95% of the cases $\beta > 2.6$ (left vertical broken line), and the median value of β equals 13. This result validates our procedure of the crossing selection and confirms that all crossings indeed belong to the CPS.

[17] It should be noted here that, since the highest energy channel of the LEP instrument was 40 keV, it could in some cases underestimate the ion temperature, especially in the innermost plasma sheet, where the average temperature is significantly higher than at larger distances. However, an estimate of the related error, based on assumption of an isotropic Maxwellian distribution of the CPS ions, shows that the error remains within 5%, provided the temperature does not exceed ~8 keV. As shown below (Figure 9), this is indeed the case within the range of geocentric distances and solar wind parameters, covered by the derived model approximations.

3. Analytical Approximations of the Plasma Sheet Parameters and Fitting Results

[18] We represent the spatial distribution of the CPS parameters in polar coordinates $\{\rho, \phi\}$, where $\rho = (X_{GSM}^2 + Y_{GSM}^2)^{\frac{1}{2}}$ is the distance from the Z_{GSM} axis and $\phi = -\tan^{-1}(Y_{GSM}/X_{GSM})$ is the azimuthal angle measured from the midnight meridian (positive in the dusk sector). Based on global patterns of the CPS density, temperature and pressure, derived in previous studies [*Spence et al.*, 1989; WN98] and in our preliminary survey of the Geotail data, the model expansions were constructed here as linear combinations of terms, approximating the radial and azimuthal variation of the CPS parameters using factors ρ^α, $\exp(-\beta\rho)$, $\sin\phi$, and $\sin^2\phi$, where α and β are free parameters. To include the effects of the solar wind and IMF conditions, the coefficients used here were also functions of appropriate parameters of the interplanetery medium. By experimenting with different expressions representing T, N, and P, the three characteristics of the CPS, we narrowed down our choice to the ones providing the best correlation between the model output and the data.

[19] Because of random fluctuations in the data, the number of terms in each expansion was limited, and increasing it further only gave marginal improvement. As shown below, different CPS parameters exhibited different amount of random scatter, and this in turn gave each a different "goodness of fit". For that reason, functional forms for each of the three parameters were devised separately, according to individual properties of the quantity under study. Many trial runs with various approximating forms were made, and decisions to retain, drop, or modify individual terms were made, based on the overall rms deviation of the model, relative magnitudes of the coefficients, and their error estimates. The model parameters were computed iteratively, using an efficient simplex minimization algorithm for the nonlinear parameters, combined with a standard inversion technique for the linear ones. After reaching a minimum of the rms deviation, the parameter search concluded with an evaluation of the statistical properties of the obtained approximation, including the errors and correlations between individual parameters. More details on the statistical theory used in the data-based modeling can be found elsewhere [*Tsyganenko*, 1990, Appendix].

3.1. Representing the Plasma Sheet Ion Temperature

[20] The CPS ion temperature T was calculated from two diagonal components of the temperature tensor $\hat{\mathbf{T}}$, provided by the DARTS website, as their average $T = (T_{yy} + T_{zz})/2$. In our data set, the observed values of T covered a wide range, from 250–300 eV to 10 keV and higher, and the overall rms temperature $\langle T \rangle$ equaled 3.79 keV.

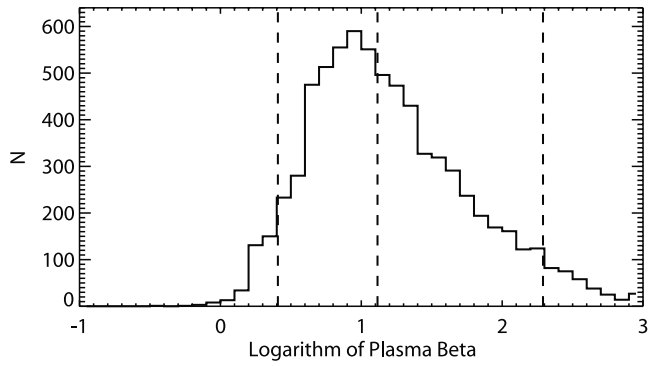

Figure 4. A histogram of the logarithm of the plasma beta parameter, calculated for the final crossing data set used in this study. Three vertical dashed lines correspond to the 5% (left), 50% (center), and 95% (right) levels.

[21] As the first step toward an analytical model we tried the simplest form, describing only an average spatial distribution of T (in keV), regardless of the solar wind state

$$T = A_1 + A_2 \exp(-A_3\rho^*), \tag{2}$$

where the radial distance was conveniently represented by a normalized variable $\rho^* = \rho/10\ R_E$. The form (2) yielded an rms deviation of the model temperature from the observed one of σ_T = 1.73 keV (46% of $\langle T \rangle$), and a correlation coefficient R_T = 0.51.

[22] The next step was to include a dependence on the solar wind conditions. By experimenting with different parameters of the interplanetary medium, it was found that adding a dependence on the solar wind speed V_{sw} in (2) yielded the greatest improvement of the fit. As the next approximation we therefore used a form with 6 free parameters A_1–A_6:

$$T = A_1 V_{sw}^{*\,A_4} + A_2 V_{sw}^{*\,A_5} \exp\left(-A_3 V_{sw}^{*\,A_6}\rho^*\right), \tag{3}$$

where the solar wind speed was also normalized as $V_{sw}^* = V_{sw}/500$ km/s. The above modification resulted in a decrease of σ_T to 1.59 keV and an increase of the correlation R_T to 0.61.

[23] Contrary to expectation, adding a similar dependence on the solar wind thermal speed did not give any notable increase of the approximation quality. However, a significant further improvement was achieved by including IMF-related terms. The best results were obtained by using the IMF B_z component as a driving variable, and it was also found that the effect of B_z was quite different for its northward and southward orientations. That prompted us to split the term with the IMF B_z into two separate terms containing its northward $B_N = B_z H(B_z)$ and southward $B_S = -B_z H(-B_z)$ parts, where H is the Heaviside function. The best-fit value of the power index A_4 of the solar wind speed V_{sw}^* was found to be close to unity, and to reduce the number of free parameters, this index was fixed at 1 in further refinements of the approximation. After that modification, σ_T dropped to 1.51 keV and the correlation coefficient R_T rose to 0.66.

[24] The final major extension of the model was made by adding a second group of terms, similar to the first one, but with a factor $\sin^2\phi$, representing a symmetric variation of the temperature from midnight toward dawn and dusk flanks of the CPS. IMF-related terms were also included in the arguments of the exponent in (3). The final adopted form for the CPS temperature was

$$T = A_1 V_{sw}^* + A_2 B_N^* + A_3 B_S^* + A_4 \exp\left[-\left(A_9 V_{sw}^{*\,A_{15}} + A_{10} B_N^* + A_{11} B_S^*\right)(\rho^* - 1)\right] + \left\{A_5 V_{sw}^* + A_6 B_N^* + A_7 B_S^* + A_8 \exp \cdot\left[-\left(A_{12} V_{sw}^{*\,A_{16}} + A_{13} B_N^* + A_{14} B_S^*\right)(\rho^* - 1)\right]\right\} \sin^2\phi, \tag{4}$$

where we used $\rho^* - 1$ instead of ρ^* just in order to keep the coefficients within a convenient range of numerical values. The IMF-related variables in (4) were also normalized using a typical average IMF magnitude (5 nT): $B_N^* = B_N/5$ nT and $B_S^* = B_S/5$ nT, so that the values of regression coefficients clearly reflected the relative importance of different terms in (4). That modification drove σ_T down to 1.42 keV and increased the correlation coefficient R_T to 0.71.

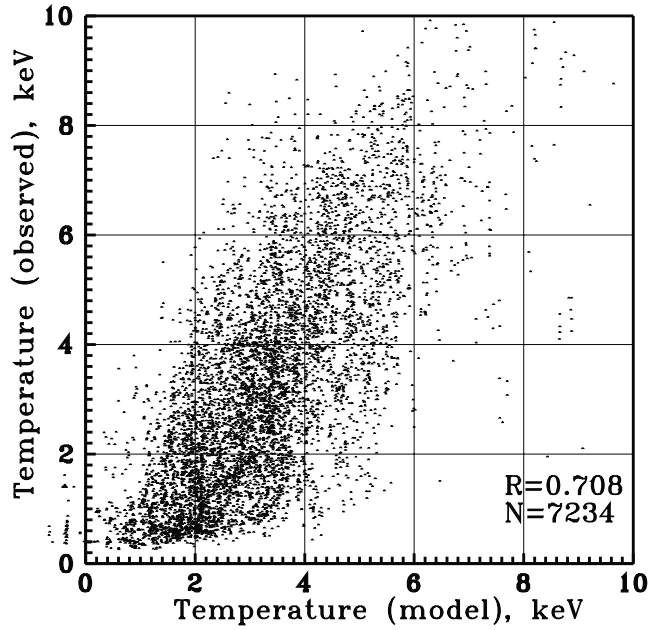

Figure 5. Scatter plot of the model values of the CPS ion temperature against the observed ones.

[25] To detect any possible dawn-dusk asymmetry of the CPS temperature, we tried adding a similar group of terms, but with a factor $\sin\phi$ instead of $\sin^2\phi$. However, several trial runs with different possible forms of the asymmetric term eventually made us conclude that the dawn-dusk asymmetry of T, if any, was confined to a narrow interval ($\sim$1 R_E) of the radial distance near the inner boundary of the modeling region at ρ = 10 R_E. Because of the large inward gradient of T in this region, combined with a considerable level of fluctuations and relative scarcity of data near the Geotail perigee, the fitting algorithm was unable to unambiguously resolve the dawn-dusk asymmetry. Typically, in the course of the iterative fitting, the coefficients in the power index of the corresponding exponential term grew quite large, so that the e-folding distance shrank to a fraction of R_E. For that reason, the approximation (4) was retained as a final model of the CPS temperature, and the dawn-dusk asymmetry was not further pursued. A more detailed discussion of this subject is given in section 5 below. Figure 5 shows a scatter plot of the observed values of T against those predicted by the model, illustrating the overall quality of the model fit.

[26] Best-fit values of the coefficients and nonlinear parameters entering in (4) are given in Table 1, along with some statistical characteristics of the CPS ion temperature. The table also provides estimates of the errors of the model parameters, calculated on the assumption that both the random component in the measured values of T and the model parameters themselves have a normal distribution around their most probable values. Both these assumptions are questionable and hard to verify, and, hence, the values of the errors in Table 1 are just rough order-of-magnitude estimates.

Table 1. Characteristics of the Data Set and of the CPS Model Parameters in Equations (4)–(6)

Parameter	Temperature T	Density N	Pressure P
Average	$\langle T \rangle$ = 3.795 keV	$\langle N \rangle$ = 0.625 cm^{-3}	$\langle P \rangle$ = 0.229 nPa
Model rms deviation	1.422	0.342	0.0427
Correlation	0.708	0.567	0.955
Equation number	(4)	(5)	(6)
A_1	1.678 ± 0.17	−0.159 ± 0.17	0.057 ± 0.023
A_2	−0.1606 ± 0.13	0.608 ± 0.17	0.524 ± 0.021
A_3	1.669 ± 0.16	0.5055 ± 0.052	0.0908 ± 0.015
A_4	4.820 ± 0.16	0.0796 ± 0.051	0.527 ± 0.630
A_5	2.855 ± 0.49	0.2746 ± 0.022	0.078 ± 0.035
A_6	−0.602 ± 0.24	0.0361 ± 0.026	−4.422 ± 1.55
A_7	−0.836 ± 0.23	−0.0342 ± 0.033	−1.533 ± 0.030
A_8	−2.491 ± 0.39	−0.7935 ± 0.060	−1.217 ± 0.14
A_9	0.2568 ± 0.023	1.162 ± 0.081	2.54 ± 1.24
A_{10}	0.2249 ± 0.060	0.4756 ± 0.14	0.32 ± 0.19
A_{11}	0.1887 ± 0.068	0.7117 ± 0.050	0.754 ± 0.017
A_{12}	−0.4458 ± 0.048		1.048 ± 0.12
A_{13}	−0.0331 ± 0.044		−0.074 ± 0.32
A_{14}	−0.0241 ± 0.041		1.015 ± 0.25
A_{15}	−2.689 ± 0.16		
A_{16}	1.222 ± 0.17		

[27] Another factor that could affect the error estimates is the degree of independence of individual measurements in the consecutive data records. In many cases, the data records selected for our set represented either multiple crossings of the same current sheet or a single traversal of a multiple structure with several current sheets located relatively close to each other. For that reason, many data records were clustered into the same relatively narrow time interval, 15–20 min or shorter. Usually, however, the solar wind parameters and the state of the CPS change much more slowly, which means that the consecutive data points within each cluster were not quite independent of each other. Therefore, since the statistical uncertainties are inversely proportional to the square root of the number of independent measurements, the uncertainties given in Table 1 should, in fact, be viewed as lower estimates of the actual ones.

3.2. Representing the Ion Density

[28] The ion density N was found to be the most unstable characteristic of the CPS, fluctuating within a wide range of values, between ~0.04 and ~6 cm^{-3}. A general trend is a monotonic decrease with growing distance from Earth. Because of the very large scatter in the data, there was little sense in retaining a free term in the analytic form for N, like A_1 in the initial approximation (2) for the temperature, and the radial decrease of N was described by a single power function of the normalized distance ρ^*. For the same reason, we did not introduce any parametric dependence on the solar wind and IMF conditions in the power index of that function, as was done for the temperature (equation (4)). The local time variation of N was described by a similar group of terms, multiplied by a common factor $\sin^2 \phi$, to represent a symmetric variation of the density in the azimuthal direction.

[29] The coefficients were represented as linear combinations of various solar wind parameters, and it was quickly determined that the principal external factor, providing the largest contribution to the CPS density, was the solar wind ion density N_{sw}. Attempts to combine N_{sw} with variable powers of the solar wind speed V_{sw} only worsened the approximation. Another factor which could potentially affect the CPS density was the IMF, and one might conjecture that the increase of the convection efficiency during the periods of southward IMF should result in larger CPS densities. Accordingly, several combinations including IMF B_z, B_S, $B_\perp \sin(\theta/2)$, $V_{sw}B_S$, etc., were tried (where $B_\perp$ is the IMF component, transverse to the Sun-Earth line, and θ is the IMF clock angle). Contrary to expectation, the largest effect was found to be produced by the northward component of the IMF, B_N, and the corresponding coefficient was positive; in other words, the CPS becomes denser during times of northward IMF. To a lesser extent, the density was also affected by the IMF southward component B_S, multiplied by the solar wind speed V_{sw}; however, the sign of the corresponding regression coefficient turned out negative, indicating a decrease of the CPS density during disturbed periods. We will address these results in more detail in section 4.2.

[30] As in the case of the temperature, no evidence was found in any trial run of a significant dawn-dusk asymmetry in the CPS density. That was not surprising, in view of the very large noise level in the data. The final form adopted for this parameter was

$$N = \left(A_1 + A_2 N_{sw}^{*A_{10}} + A_3 B_N^* + A_4 V_{sw}^* B_S^*\right)\rho^{*A_8} + \left(A_5 N_{sw}^{*A_{11}} + A_6 B_N^* + A_7 V_{sw}^* B_S^*\right)\rho^{*A_9} \sin^2 \phi, \quad (5)$$

where the normalized variables were defined as $N_{sw}^* = N_{sw}/10$, $B_N^* = B_N/5$, $B_S^* = B_S/5$, $\rho^* = \rho/10$, and $V_{sw}^* = V_{sw}/500$.

[31] The model parameters for the CPS ion density are given in the middle column of Table 1. Even though in most cases the errors are quite large, reflecting the large scatter in the data, the model still reveals several basic features of the observed CPS density and its response to the external input, discussed in more detail in section 4.2. Figure 6 displays a

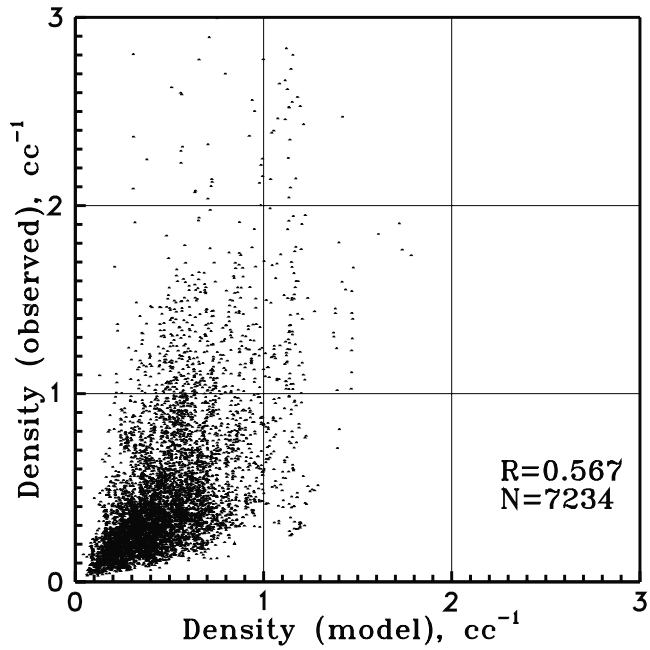

Figure 6. Scatter plot of the model values of the CPS ion density against the observed ones.

scatter plot, illustrating the overall predictive capability of the approximation (5). The correlation coefficient between the model and the data equals $R = 0.57$. As can be seen from the plot, the approximation (5) fails to predict large values of the proton density, exceeding $\sim$1 cm^{-3}.

3.3. Representing the Ion Pressure

[32] The plasma pressure is probably the most interesting and important characteristic of the CPS, because it is closely related to the configuration of the magnetic field by the requirement of approximate force balance. In particular, the spatial gradient of the plasma pressure is an important factor in the magnitude and polarity of the Birkeland currents, a principal element of the coupling between the ionosphere and magnetosphere. From force balance considerations, one also might intuitively expect that the solar wind pressure is the main factor determining the particle pressure in the CPS.

[33] This conjecture has been fully confirmed in our trial calculations, using various functional forms with different external driving parameters. In all cases, the highest correlation with observations and the lowest rms error was obtained with the ram pressure of the incoming solar wind (in nanopascals), $P_{sw} = 1.94 \cdot 10^{-6} N_{sw} V_{sw}^2$ as the driving factor. Here the numerical coefficient assumes that α-particles on the average constitute 4% of the solar wind proton number density N_{sw} (in cm^{-3}), and the solar wind speed V_{sw} is in km/s. The IMF also played a role, yet was not as important as the solar wind ram pressure. From various possible combinations of IMF-related quantities, the parameter $F = B_\perp \sqrt{\sin(\theta/2)}$ yielded the best results. Like in the case of the CPS temperature, only a token improvement (about 0.5%) was gained by adding a term with the solar wind thermal pressure, and that variable was not included in further numerical experiments.

[34] An analytical approximation for the CPS pressure was constructed using basically the same approach as for the temperature and the density. However even in the initial tentative runs, it became clear that the CPS ion pressure $P = NT$ was a remarkably stable and ordered parameter, in a dramatic contrast with its constituent factors, N and T. That manifested itself in surprisingly high values of the correlation coefficient between the data and model approximations.

[35] The following form was adopted as a final approximation for the pressure

$$P = A_1 \rho^{*A_6} + A_2 P_{sw}^{*\,A_{11}} \rho^{*\,A_7} + A_3 F^{*\,A_{12}} \rho^{*\,A_8} + \left[A_4 P_{sw}^{*\,A_{13}} \cdot \exp(-A_9 \rho^*) + A_5 F^{A_{14}} \exp(-A_{10} \rho^*)\right] \sin^2 \phi, \quad (6)$$

where the solar wind ram pressure and the IMF parameter F were also normalized to their typical average values (3 nPa and 5 nT), so that $P_{sw}^* = P_{sw}/3$ and $F^* = F/5$. Unlike in the equation (5) for the temperature, the power functions of ρ^* were used in the purely radial part of (6) (first 4 terms), since they yielded slightly better results than exponents, and it also proved more accurate to use separate terms with different power indices for ρ^*, P_{sw}^*, and F^*.

[36] In the same way as for the ion temperature and density, an attempt was made to detect and evaluate a possible dawn-dusk asymmetry of the pressure, by adding a group of terms with a flexible radial variation and a common factor sin ϕ. However, as in the former cases, no tangible asymmetry was found anywhere except in a very thin layer at the inner boundary $\rho = 10\ R_E$ of the modeling region. Most likely, that was an artifact of the rapid inward growth of the pressure and its radial gradient, a much larger fluctuation level, and fewer data. It should also be noted that, while dawn-dusk asymmetries of T and N might well exist in the near CPS, it is possible that we could not detect them due to their large fluctuation. In contrast, the CPS pressure P is much more stable; therefore, if a persistent large-scale asymmetry had indeed existed, it would have readily shown up in our fitting runs. Hence, the negative result indicates that the dawn-dusk asymmetry of the CPS pressure is really insignificant beyond 10 R_E, which is consistent with the observed symmetry of the tail lobe magnetic field.

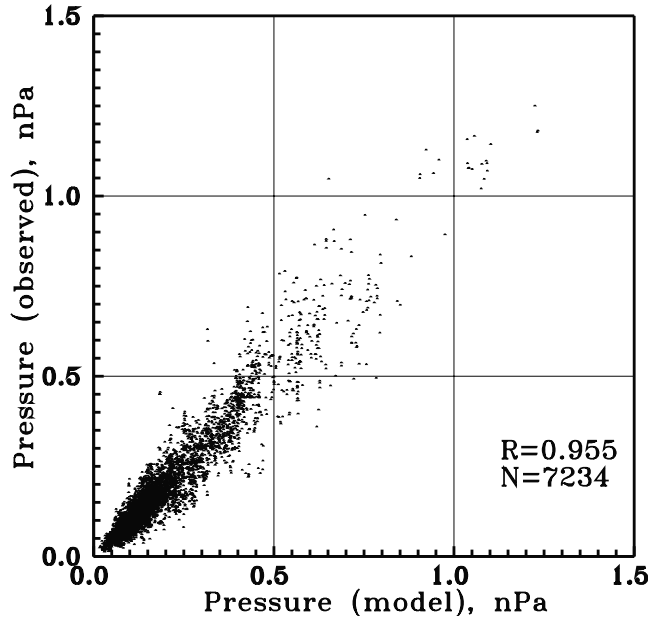

Figure 7. Scatter plot of the model values of the CPS ion pressure against the observed ones.

[37] The model parameters A_1–A_{14} entering in (6) are given in the right column of Table 1 together with their error estimates. Figure 7 shows the corresponding scatter plot, illustrating the high correlation (R = 0.955) between the model's output and the actual observed CPS pressure.

4. Spatial Distribution of the CPS Parameters and Their Response to the Solar Wind and IMF Conditions

[38] Information that can be derived from data-based models is naturally limited by the spatial extent of the data, used in the derivation of model parameters. As discussed in section 2 and shown in Figure 2, the largest spatial density of the Geotail observations in our data set was between the radial distances 10 and 30 R_E, with much fewer data in the interval between 30 and 50 R_E. Extrapolating the derived approximations in the inner magnetosphere ($R < 10\ R_E$) and in the far tail ($R > 50\ R_E$) may yield unpredictable and physically incorrect results.

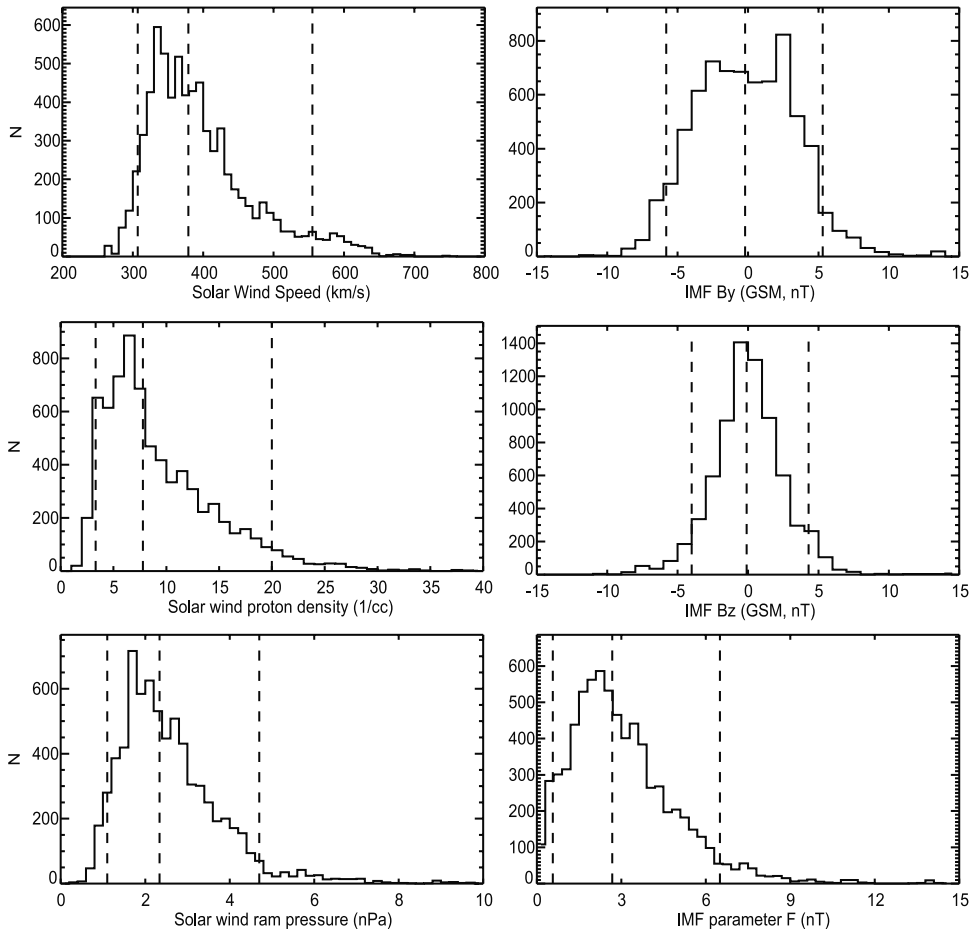

Figure 8. Histograms illustrating the coverage by the data of the parametric space of the solar-wind and IMF-related variables.

[39] One should also be aware of the limited coverage by our data of the range of possible solar wind and IMF conditions and, hence, of inevitable limitations on acceptable values of input parameters. For that reason, before analyzing the modeling results, we start this section by a brief survey of the data coverage in the parametric space of the input variables entering in (4)–(6).

[40] Figure 8 shows distributions of the values of the solar wind and IMF parameters used, either directly or indirectly, in the calculation of the input variables for the approximations (4)–(6). On each of the six panels, three vertical dashed lines correspond to the 0.05, 0.50, and 0.95 levels, so that 90% of the records in our data set fall within the interval between the left and right lines. The middle dashed line in all the plots indicates the median values. As can be seen from the histograms, our data set provides a fair coverage of the average conditions, but contains very few data with unusually fast and dense solar wind, and/or strongly southward/northward IMF. This is a common problem in any kind of the data-based modeling, naturally caused by the relative rarity of unusual events (in our case - strong disturbances at the Sun and in the solar wind).

4.1. CPS Ion Temperature

[41] As shown in section 3.1, the CPS temperature can be quantitatively best described by using the solar wind speed V and the IMF B_z as principal driving parameters. To visualize the impact of the state of the interplanetary medium on the CPS temperature, we plotted color-coded maps of $T = T(x, y)$, for values of V and B_z close to their 5% and 95% levels in the histograms shown in Figure 8. Comparison of the graphs clearly illustrates the effect of changing individual input parameters, without transcending too far the limits of the model's validity.

[42] Figure 9 displays four panels; the upper and lower rows correspond, respectively, to the lower and upper levels of the solar wind speed, $V_{sw} = 300$ km/s and $V_{sw} = 600$ km/s. The left and right columns correspond to the opposite polarities of the IMF B_z, equal to +5 nT and −5 nT, respectively. In all cases, the ion temperature rapidly falls off with growing geocentric distance. Another clear and persistent feature is that the temperature peaks at the midnight meridian and decreases toward the dawn and dusk flanks of the PS. The azimuthal variation becomes more pronounced with growing tailward distance.

[43] Larger (smaller) solar wind speed results in hotter (cooler) CPS and, as can be seen from the maps, this effect is somewhat stronger at larger distances and for positive IMF B_z. Negative IMF B_z raises the CPS temperature over the entire region under study, whereas positive B_z values drive the temperature down, with the strongest effect near the tail's boundary. The steep decrease of T near the

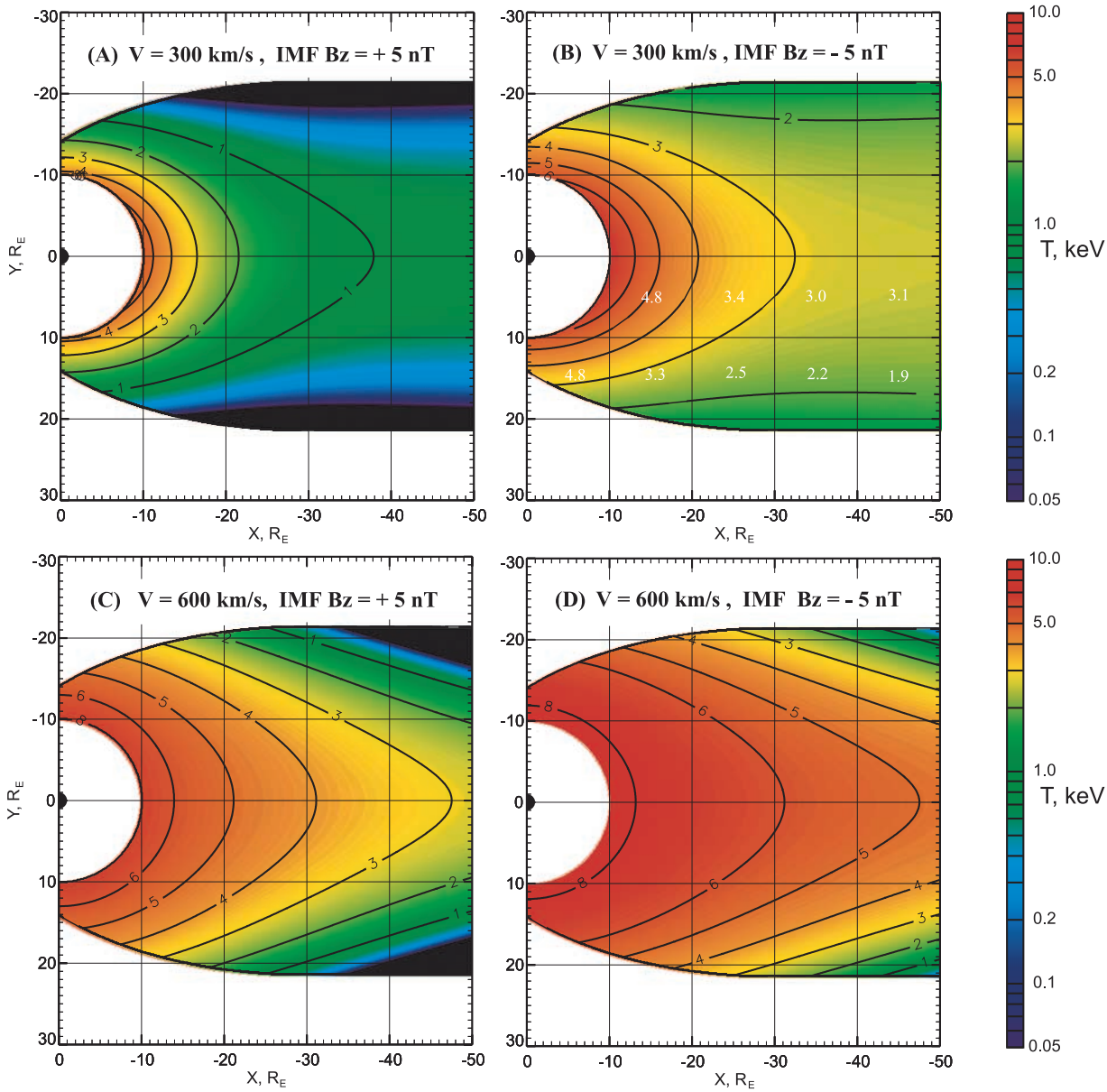

Figure 9. (a–d) Color-coded plots of the CPS ion temperature given by (4), corresponding to lower and upper limits of the solar wind speed and IMF B_z. Values shown in white color in the top right panel are those of the rms deviation σ_T for individual 10-R_E bins of X and Y.

boundary may well be an artifact of the expansion (4) which, because of the strong scatter in the data (Figure 5) had to be limited here to a simple form, with a single azimuthally varying term, proportional to $\sin^2 \phi$ and linear with respect to B_z. As a result, for large and positive values of the IMF B_z, the model temperature becomes even negative near the magnetopause (black regions in the left panels in Figure 9). Another obvious cause of this unphysical feature was the lack of Geotail data in that region, as can be clearly seen in Figure 2 (left panel).

[44] To quantify the variability of the CPS parameters as a function of position, Figure 9 also shows the values σ_T of the rms deviation of the model values of T from the observed ones, calculated separately for 9 bins of X and $|Y|$ with $\Delta X = \Delta Y = 10\ R_E$. To avoid overcrowding of the figures by redundant information, they are shown in only one of the four panels (top right), but actually refer to the model in general (i.e., are based on the entire data set), and should not be associated with the particular values of the model input parameters, shown on top of that panel. Note also that, based on the assumed symmetry of the model T with respect to the midnight meridian plane, the data were "folded" about that plane. In other words, the CPS crossings were actually binned according to their $|Y|$ values, rather than Y, so that data from the postmidnight sector (with negative Y) were added into the corresponding premidnight bins. As seen from the figure, σ_T behaves, in general, similarly to the temperature itself: it increases sunward and from the flanks to the center of the CPS.

4.2. CPS Ion Density

[45] Figure 10 displays four panels with the maps of the CPS ion density, similar in format to those for T in Figure 9. Here the input drivers are the solar wind proton density N_{sw} and the IMF B_z. Equation (5) also included the solar wind speed V_{sw}, but it entered only as a modifying factor to the IMF B_z, for southward IMF conditions. As in the previous case, the values of both input parameters were chosen close to their 5% and 95% levels, 3 cm^{-3} and 20 cm^{-3} for $N_{\rm sw}$, and +5 nT and −5 nT for IMF B_z. The solar wind speed was assumed here equal to its average value of 380 km/s.

[46] Near the tail's axis, the CPS density decreases downtail; however, the rate of its radial fall-off sharply decreases away from the midnight meridian, due to a pronounced increase of the density from the tail's center toward its dawn and dusk flanks. That feature is clearly seen in all four panels, with a significantly larger effect in the case of high solar wind density (bottom).

[47] The solar wind ion density has obviously the largest impact on the CPS density, although the response is not linear: a nearly 7-fold increase in $N_{\rm sw}$ causes a more modest increase of the ion content inside the CPS, by a factor of ~1.5–3. The relative sensitivity to changes in $N_{\rm sw}$ is somewhat larger for negative IMF B_z. The IMF B_z itself has a negative correlation with the CPS density, so that negative (positive) B_z results in a less (more) dense plasma sheet. An obvious interpretation is that during the periods of negative IMF B_z the near-Earth PS is heated by the greater energy flow from the solar wind into the magnetosphere, which requires a decrease in the density, to ensure a relatively stable PS pressure.

4.3. CPS Ion Pressure

[48] The CPS ion pressure is controlled in our approximations by the solar wind ram pressure P_{sw} and by the IMF parameter F, defined in section 3.3. According to the histograms in Figure 8, their respective 5% and 95% values are equal to 1.1 nPa and 4.7 nPa for $P_{\rm sw}$, and 0.6 nT and 6.5 nT for F. In terms of the solar wind speed and density, the above values of $P_{\rm sw}$ approximately correspond to (for example) $V_{\rm sw}$ = 300 km/s and $N_{\rm sw}$ = 6 cm^{-3}, and $V_{\rm sw}$ = 500 km/s and $N_{\rm sw}$ = 10 cm^{-3}, respectively. The simplest choice of the IMF components, providing $F = -0.6$ and $F = 6.5$, is a strictly southward IMF with $B_z = -0.6$ nT and $B_z = -6.5$ nT.

[49] Figure 11 shows four color-coded distributions of the pressure, corresponding to four combinations of the above parameters, indicated on the top of each plot. As can be seen by comparing the upper and lower panels, an almost 3-fold increase of the solar wind dynamic pressure results in roughly the same relative increase of the CPS pressure, the effect being somewhat stronger for the smaller value of the IMF parameter F. Larger values of F (which could result not only from greater southward IMF B_z, but also from larger absolute values of B_y) cause a general increase of the CPS pressure, more pronounced for lower values of the solar wind pressure.

[50] Another interesting effect of the IMF, with a clear physical interpretation, is a change in the shape of the contours of equal P. As can be seen by comparing two top panels in Figure 11, the contours in the left panel, plotted for $F = 0.6$, are closer to circles than in the right one, corresponding to a strong southward IMF B_z with $F = 6.5$. This produces a more rapid transition with growing radial distance, from the quasi-dipolar field structure to the tail-like configuration, with a magnetic field highly stretched along the X axis and nearly uniform in the Y direction. Since the particle pressure in the CPS should match the tail lobe magnetic field pressure, it also should become nearly uniform across the tail. This is exactly what one sees in Figure 11b. The effect is also seen in the bottom panels, corresponding to a much higher solar wind pressure, though it is less pronounced there.

5. Discussion

[51] The principal goal of this work was to derive simple quantitative approximations for the main parameters of the ion component of the CPS, as functions of the position $\{X, Y\}$ on the nightside, and their response to conditions in the incoming solar wind. From the viewpoint of magnetospheric modeling, the plasma pressure P is the most important parameter among those addressed in this paper, since it is closely associated with the dynamics and structure of the magnetic field, via the requirement of approximate stress balance in the system. It should be noted that the approximations devised here describe only the ion component of the CPS; to obtain the full pressure, one should add a contribution from electrons, which varies between 10% and 20% of the ion pressure.

[52] Based on data of the ISEE-2 Fast Plasma Experiment, *Borovsky et al.* [1998] made a study of the solar wind control of the ion temperature and density at two locations in the PS (in the central tail and at geosynchronous orbit). They also reported a significant correlation of the PS temperature and density with the solar wind speed and density, respectively. The effect of the IMF orientation was addressed earlier by *Terasawa et al.* [1997] and *Fujimoto et al.* [1997]. They found that the plasma sheet becomes significantly cooler and denser during prolonged intervals of northward IMF, and that the cold-dense plasma regime is the most pronounced near the tail's flanks. A similar conclusion was also made recently by *Wing and Newell* [2002]. Our results are consistent with those findings and provide a quantitative description of the spatial distribution of the plasma sheet parameters and their dependence on the state of the solar wind and IMF.

[53] As we have seen above, reliable model approximations for the ion temperature T and the density N were hampered by the enormous scatter in the data for both of these parameters. In contrast, their product $P = NT$ showed a remarkable coherence and stability, readily understandable from basic principles of plasma physics. The distribution of T and N in the CPS, unlike that of P, reflects a multitude of very complex processes with different spatial and time scales, involving plasma irregularities in the incoming solar wind, large-scale turbulence and instabilities in the magnetosheath, LLBL, and in the PS itself, including intermittent magnetic reconnection, plasmoids, flux ropes, injection of ionospheric particles, and so forth. The observed irregularity of T and N in a parcel of tail plasma is a result of its entire history, from its entrance into the PS to its arrival at Geotail's location via convective transport.

[54] In contrast, the plasma pressure distribution is controlled and maintained in an (approximate) equilibrium via a much faster agent, providing an efficient communication between different regions of the magnetosphere and with the solar wind. That agent is fast magnetosonic waves,

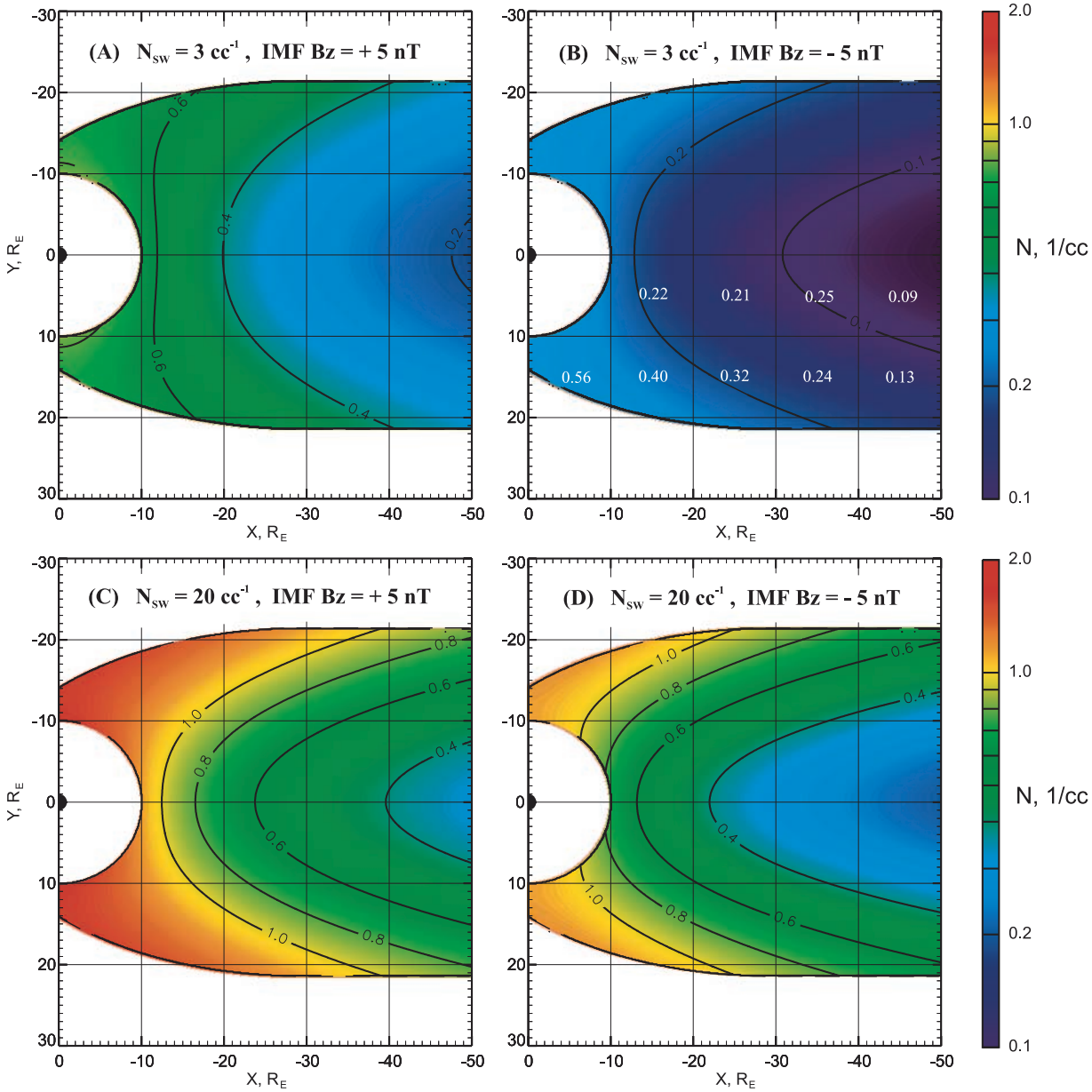

Figure 10. (a–d) Color-coded plots of the CPS ion density given by (5), corresponding to lower and upper limits of the solar wind ion density and IMF B_z. The solar wind speed V_{sw} = 380 km/s. Values shown in white color in the top right panel are those of the rms deviation σ_N for individual 10-R_E bins of X and Y.

which rapidly propagate information on the changing solar wind state inside the magnetosphere and establish an orderly force-balanced configuration.

[55] Concerning the issue of the force balance, it is interesting to compare the above results for the plasma pressure with independent model results on the tail lobe magnetic field, as well as with previous statistical studies of the PS pressure. The tail lobe field can be derived in a straightforward way from the T96 model [*Tsyganenko*, 1995, 1996], since it accepts the same input parameters as our approximation (6).

[56] At distances beyond ~20 R_E, the average magnetotail structure becomes nearly one-dimensional, owing to the much slower flaring of the tail boundary and smaller radial gradient of the lobe magnetic field B_{lobe}. That allows one to easily relate there the CPS pressure P and $B_{\rm lobe}$, using the condition of the transverse pressure balance, $P = \mu_0 B_{\rm lobe}^2/2$. In the near magnetosphere ($R < \sim 20\ R_E$), the magnetic structure is more complicated because of the rapidly growing contribution from the Earth's dipole, increasingly non-uniform and stronger magnetopause field, and a significant earthward gradient of the cross-tail current. The configuration of the near magnetotail is therefore no longer one-dimensional. For that reason, the problem of self-consistently relating the plasma pressure with the ambient magnetic field is much more difficult here (and probably has no unique solution). *Spence et al.* [1987] and *Toffoletto et al.* [2000] gave a more detailed treatment of that subject and devised numerical procedures to derive a plasma pressure, approximately consistent with a model magnetic field.

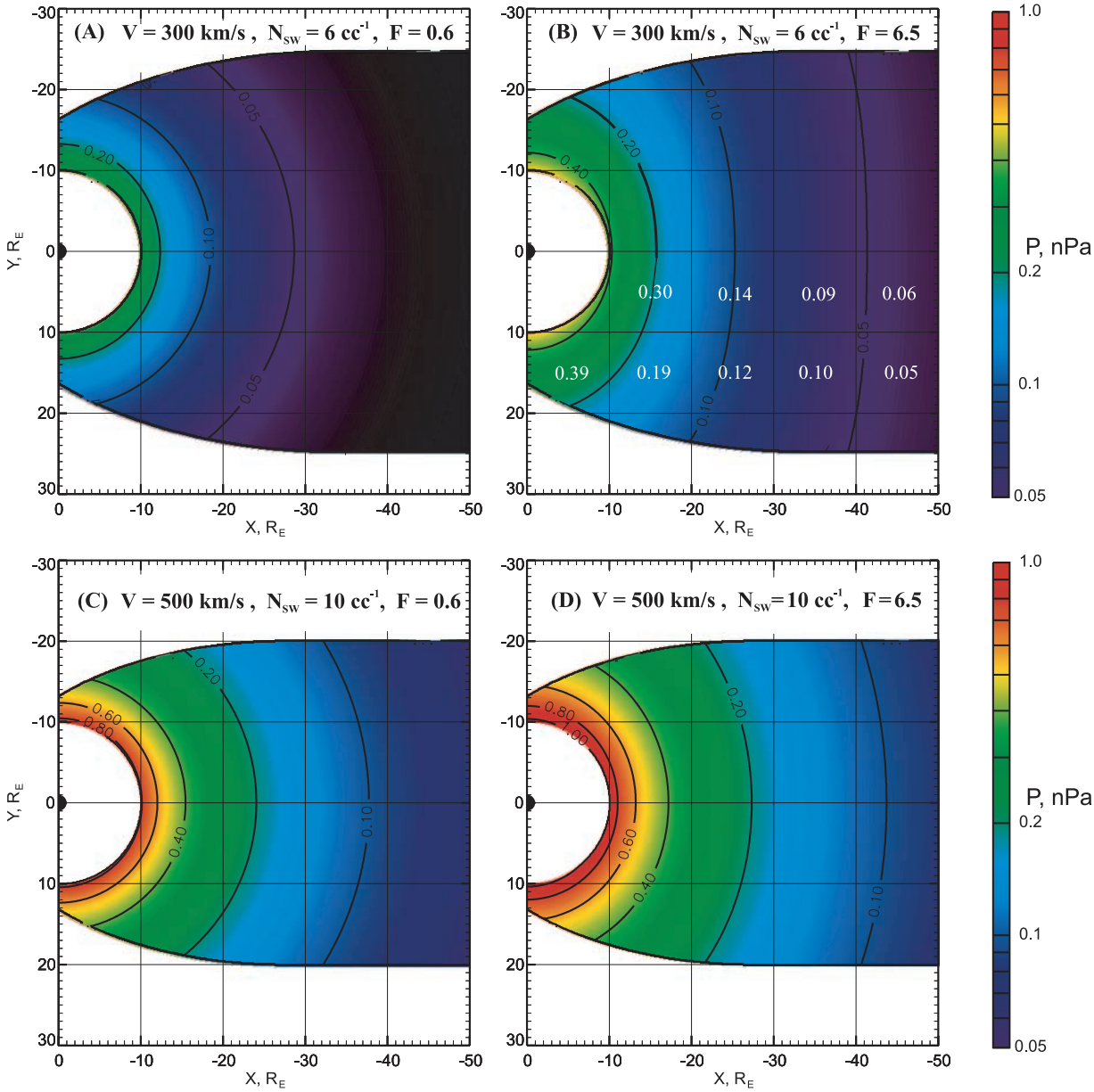

Figure 11. (a–d) Color-coded plots of the CPS ion pressure given by (6), corresponding to lower and upper limits of the solar wind ram pressure and the IMF-related parameter F. Values shown in white color in the top right panel are those of the rms deviation σ_P for individual 10-R_E bins of X and Y.

[57] In this work we do not attempt to go that far, and only make a rough estimate of the consistency of the data-based model pressure with a model magnetic field. From qualitative considerations, it is obvious that using the total model field (i.e., including the Earth's dipole contribution) in the transverse pressure balance equation $P = \mu_0 B_{\rm lobe}^2/2$ would overestimate the CPS pressure on the left-hand side. Using only the external part of the model magnetic field (without the dipole) might be better, although it's likely to underestimate the pressure near the inner edge of the plasma sheet. With these caveats in mind, we calculated and presented in Figure 12 radial profiles of the tail lobe field, obtained using the same 4 combinations of the solar wind and IMF parameters as those in Figure 11. Each panel displays (a) two curves (dashed lines), corresponding to the total and external T96 model field (with and without the Earth's dipole field, respectively), (b) the equivalent lobe field $B_{\rm lobe} = (2P/\mu_0)^{\frac{1}{2}}$ based on the present model (equation (6); heavy solid line), and (c) the same field but derived from an average quiet-time pressure profile, given by the approximation of *Spence and Kivelson* [1993] (thin solid line).

[58] As can be seen from the plots, the equivalent lobe field $B_{\rm lobe}$ agrees quite well with that from the T96 model, especially for low values of the IMF index F (two panels on the left). As expected, in the innermost region ($R \sim 10\ R_E$) $B_{\rm lobe}$ falls between the upper and lower estimates given by the T96 field model. The agreement is somewhat worse for $F = 6.5$ (two panels on the right): in the limit of low ram pressure ($V_{\rm sw}$ = 300 km/s, $N_{\rm sw}$ = 6 cm^{-3}, panel B), the equivalent lobe field exceeds the T96 field in the distant tail, but falls short of it in the near tail, in the high-pressure

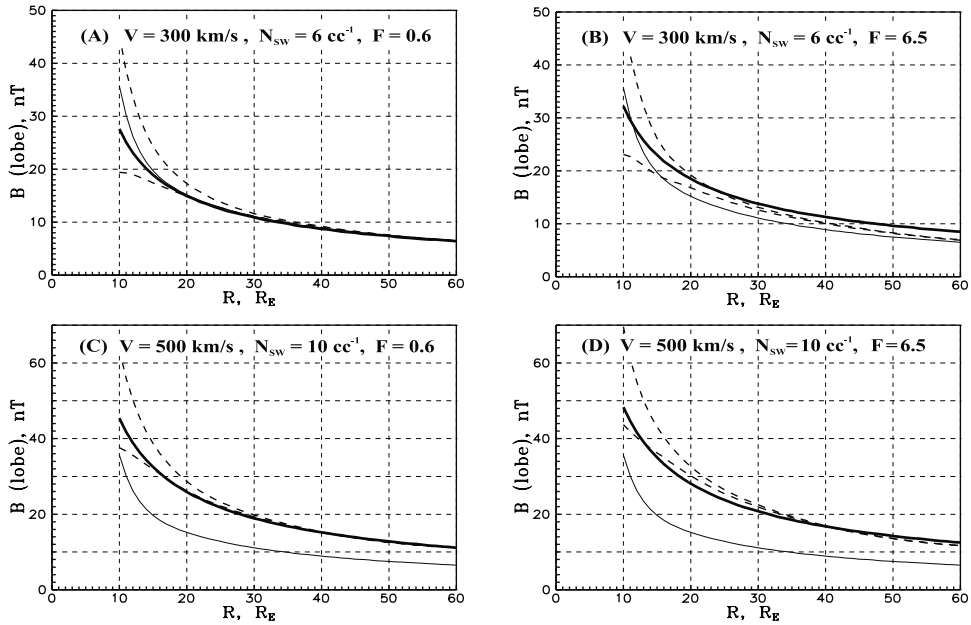

Figure 12. (a–d) Comparing the radial profiles of the tail lobe magnetic field in the T96 model (dashed lines; see text for details) with an equivalent lobe field, calculated using the present approximation for the CPS ion pressure (thick solid line). For comparison, the equivalent lobe field for the quiet-time approximation of *Spence and Kivelson* [1993] is shown on each panel by a thin solid line.

limit. The discrepancies are relatively small, and can be attributed to many factors, pertaining both to the data and to the model approximations, used for the T96 and in the present CPS model. Based on the estimates of the errors of the model parameters (Table 1), one can expect the values of P given by (6) to be accurate within 7–8%, while the model tail lobe field deviates from the observed one, typically, within 10–12% of its rms value, so the obtained discrepancies are not at all disturbing.

[59] It should be noted, that the equivalent lobe field $B_{\rm lobe}$ did not take into account the contribution of electrons to the total pressure. As mentioned in the beginning of this section, the electron component usually accounts for 10–20% of the total energy density. In terms of the equivalent lobe field, this yields a 5–10% increase above the values based only on ions. Such a correction is also within the accuracy of the comparison in Figure 12.

[60] In the beginning of this paper we mentioned an effort by WN98 to derive similar 2-D maps of the CPS parameters, based on low-altitude particle data and a model mapping. No attempt was made here to compare in detail our results with those maps, mostly, because of the completely different scheme of parameterization adopted in our works. While we used solar wind and IMF parameters as controlling variables, WN98 employed an index (MT) of the near magnetotail stretching, and there exists no direct way to uniquely relate them. However, it is still possible to compare the values of the CPS pressure for quiet conditions, represented by Figure 4 of WN98 and by Figure 11a in this work. According to the plot of WN98, in the range of distances $20 < R < 40\ R_E$ their total quiet-time CPS pressure stays at a nearly constant level above 0.25 nPa, while our model predicts a relatively steep radial decrease of P, from 0.10 at $R = 20\ R_E$ to 0.04 nPa at $R = 40\ R_E$. Even though our approximation (6) does not include the magnetic pressure and the contribution from electrons, included in WN98, those terms are only small corrections and cannot be responsible for the discrepancy, also found by *Wang et al.* [2001]. In our view, the most likely cause is using of overstretched model fields in WN98. While the correction procedure based on the MT-index could significantly improve the mapping accuracy in the immediate vicinity of the isotropy boundary ($R \sim 10$–$15\ R_E$), multiplying the entire tail field by the same correction factor could have resulted in an overestimate at larger distances, where the tail field B_z (and hence its degree of stretch) is especially sensitive to the magnitude of the cross-tail current.

6. Summary and Outlook

[61] In this paper, we presented results of an empirical modeling of the main macroscopic parameters of the Earth's magnetotail plasma sheet and their response to the solar wind and IMF conditions. The obtained approximations were based on data of Geotail plasma and magnetic field instruments, taken between 1994 and 1998, and on the concurrent interplanetary medium data of the Wind and IMP 8 spacecraft. The models are valid in the range of radial distances from 10 to 50 R_E and include the dawn-dusk variation of the plasma parameters across the magnetotail. The CPS data were identified using reversals of the radial component of the magnetic field, as an indicator of the spacecraft traversal of the CPS. In addition, LLBL and PSBL data were filtered out, by using a criterion based on the ratio of the ion temperature to their density, and by editing out the data with large flow speeds.

[62] As established from many trial runs with different regressors, the CPS ion temperature T is controlled mainly by the solar wind speed V and, to a lesser extent, by the IMF B_z. It peaks at the midnight meridian and falls off toward the

PS flanks (Figure 9). Faster (slower) solar wind flow and southward (northward) IMF B_z result in a hotter (cooler) PS. The values of the temperature, yielded by the approximation (4), correlated fairly well with the observed ones (R_T = 0.71). However, lack of data in the distant tail and a high level of fluctuations precluded us from using more flexible approximations, and the simple ones used gave negative values of the model temperature near the distant PS boundary, for northward IMF conditions.

[63] No sensible improvement of the fit was found from adding of dawn-dusk asymmetric terms in the trial expansions for *T*. Consequently, those terms were not included in the final version of the approximation (4).

[64] The CPS ion density *N* (Figure 10) was found to be controlled mostly by the solar wind proton density and by the northward component of the IMF. Being the most unstable characteristic of the CPS, it yielded the highest scatter of the observed values compared to their analytical approximation (5), and, hence, the lowest correlation between them, R_N = 0.57. In all cases, the model CPS density had a pronounced minimum at midnight and increased toward the tail's flanks. Larger (smaller) solar wind ion densities and northward (southward) IMF B_z resulted in larger (smaller) *N* in the PS. A significant asymmetry was found in the IMF impact on the density: northward IMF increased *N* much more than a southward IMF B_z of the same amplitude. As with the temperature, we could not detect any dawn-dusk asymmetry of the density, and, hence, no asymmetric terms were retained in the final approximation (5).

[65] In a dramatic contrast with the ion temperature and density, the ion pressure *P* was found to be a very well-ordered and stable parameter of the CPS. The corresponding best-fit approximation yielded a very high correlation (R_P = 0.95) with the actually observed values of *P*. No indication was found of any significant dawn-dusk asymmetry of the CPS pressure, consistent with the observed symmetry of the tail lobe magnetic field. Accordingly, no asymmetric terms were included in the final approximation (6) for the pressure. Among different driving parameters tested in the initial trial runs, the solar wind ram pressure clearly yielded the best results. A significant improvement was also obtained by adding an IMF-related term, and the highest correlation with the data was provided by using the index $F = B_\perp\sqrt{\sin(\theta/2)}$.

[66] The ion pressure *P* (Figure 11) was found to be roughly constant across the midtail ($R \sim 20-50\ R_E$); at closer distances the isobars *P* = constant gradually bent and nearly followed the contours of constant geomagnetic field. For northward IMF conditions combined with a slow solar wind, they remained quasi-circular up to much larger distances, reflecting a weaker tail current and, hence, a more dipole-like magnetic field.

[67] As already said, the obtained approximations are based on data taken at $R \geq 10\ R_E$ and, hence, become invalid in the inner magnetosphere. It would be an attractive problem to extend the present model inward, by adding to our data set particle data, taken closer to Earth, and using more sophisticated approximations. However, there exist several complicating factors, reflecting a fundamental difference between the physical characteristics of the inner magnetosphere and the plasma sheet. For one thing, the particle pressure in the inner magnetosphere becomes anisotropic and, hence, no longer remains constant along the magnetic field lines. Therefore, in order to define a 3-D distribution of the pressures $P_\parallel$ and $P_\perp$, it no longer suffices to know them in the equatorial plane: one also needs to have more detailed information on the particle distribution function (e.g., bi-maxwellian, kappa, etc.) In addition, the inner magnetospheric plasma contains a significant population of ions of terrestrial origin, especially during storms. Another complication is related to much larger magnetic field and much slower convection speeds, resulting in significantly larger time delays between the solar wind and IMF input and the response of the inner magnetosphere. These effects fall beyond the limits of the empirical approach and can be properly reproduced only by means of realistic particle simulations, representing in a self-consistent way the magnetic field and plasma dynamics.

[68] **Acknowledgments.** The authors acknowledge Tsugunobu Nagai (Tokyo Institute of Technology, Japan) for providing the Geotail MGF data via the DARTS online facility. Many thanks are also due to Yoshifumi Saito for his contribution to the LEP ion data calibration, and to Don Fairfield for his advice concerning the MGF data of Geotail. Careful reading and innumerable helpful comments on the manuscript by David Stern are gratefully appreciated. Wind and IMP 8 solar wind and IMF data were provided by NSSDC (GSFC, Greenbelt) online via the CDAWEB facility. This work was supported by NSF grants ATM-0207248 and by NASA's LWS grant NAG5-12185.

[69] Lou-Chuang Lee thanks Kazuo Shiokawa and another reviewer for their assistance in evaluating this paper.

References

Baumjohann, W., G. Paschmann, and C. A. Cattell, Average plasma properties in the central plasma sheet, *J. Geophys. Res.*, *94*, 6597, 1989.

Borovsky, J. E., M. F. Thomsen, and R. C. Elphic, The driving of the plasma sheet by the solar wind, *J. Geophys. Res.*, *103*, 17,617, 1998.

Fujimoto, M., T. Terasawa, and T. Mukai, The cold-dense plasma sheet: A Geotail perspective, *Space Sci. Rev.*, *80*, 325, 1997.

Hori, T., K. Maezawa, Y. Saito, and T. Mukai, Average profile of ion flow and convection electric field in the near-Earth plasma sheet, *Geophys. Res. Lett.*, *27*, 1623, 2000.

Huang, C. Y., and L. A. Frank, A statistical survey of the central plasma sheet, *J. Geophys. Res.*, *94*, 83, 1994.

Kaufmann, R. L., B. M. Ball, W. R. Paterson, and L. A. Frank, Plasma sheet thickness and electric currents, *J. Geophys. Res.*, *106*, 6179, 2001.

Kistler, L. M., W. Baumjohann, T. Nagai, and E. Möbius, Superposed epoch analysis of pressure and magnetic field configuration changes in the plasma sheet, *J. Geophys. Res.*, *98*, 9249, 1993.

Kokubun, S., T. Yamamoto, M. H. Acuna, K. Hayashi, K. Shiokawa, and H. Kawano, The Geotail magnetic field experiment, *J. Geomagn. Geoelectr.*, *46*, 7, 1994.

Mukai, T., et al., The low energy particle (LEP) experiment onboard the Geotail satellite, *J. Geomagn. Geoelectr.*, *46*, 59, 1994.

Nishida, A., The Geotail mission, *Geophys. Res. Lett.*, *21*, 2871, 1994.

Shue, J.-H., et al., Magnetopause location under extreme solar wind conditions, *J. Geophys. Res.*, *103*, 17,691, 1998.

Spence, H. E., and M. G. Kivelson, Contributions of the low-latitude boundary layer to the finite width magnetotail convection model, *J. Geophys. Res.*, *98*, 15,487, 1993.

Spence, H. E., M. G. Kivelson, and R. J. Walker, Static magnetic field models consistent with nearly isotropic plasma pressure, *Geophys. Res. Lett.*, *14*, 872, 1987.

Spence, H. E., M. G. Kivelson, R. J. Walker, and D. J. McComas, Magnetospheric plasma pressures in the midnight meridian: Observations from 2.5 to 35 R_E, *J. Geophys. Res.*, *94*, 5264, 1989.

Terasawa, T., et al., Solar wind control of density and temperature in the near-Earth plasma sheet: Wind/Geotail collaboration, *Geophys. Res. Lett.*, *24*, 935, 1997.

Toffoletto, F. R., R. W. Spiro, R. A. Wolf, J. Birn, and M. Hesse, Modeling inner magnetospheric electrodynamics, in *Space Weather*, *Geophys. Monogr. Ser.*, vol. *125*, edited by P. Song, H. J. Singer, and G. L. Siscoe, p. 265, AGU, Washington, D. C., 2000.

Tsyganenko, N. A., Quantitative models of the magnetospheric magnetic field: Methods and results, *Space Sci. Rev.*, *54*, 75, 1990.

Tsyganenko, N. A., Modeling the Earth's magnetospheric magnetic field confined within a realistic magnetopause, *J. Geophys. Res.*, *100*, 5599, 1995.

Tsyganenko, N. A., Effects of the solar wind conditions on the global magnetospheric configuration as deduced from data-based field models, *Eur. Space Agency Spec. Publ., ESA SP-389*, 181, 1996.

Tsyganenko, N. A., S. B. P. Karlsson, S. Kokubun, T. Yamamoto, A. J. Lazarus, K. W. Ogilvie, C. T. Russell, and J. A. Slavin, Global configuration of the magnetotail current sheet as derived from GEOTAIL, WIND, IMP-8, and ISEE-1/2 data, *J. Geophys. Res.*, *102*, 6827, 1998.

Wang, C.-P., L. R. Lyons, M. W. Chen, and R. A. Wolf, Modeling the quiet time inner plasma sheet protons, *J. Geophys. Res.*, *106*, 6161, 2001.

Wing, S., and P. T. Newell, Central plasma sheet properties as inferred from ionospheric observations, *J. Geophys. Res.*, *103*, 6785, 1998.

Wing, S., and P. T. Newell, 2D plasma sheet ion density and temperature profiles for northward and southward IMF, *Geophys. Res. Lett.*, *29*(9), 1307, doi:10.1029/2001GL013950, 2002.

T. Mukai, Institute of Space and Astronautical Science, 3-1-1 Yoshinodai, Sagamihara, Kanagawa 229-8510, Japan. (mukai@stp.isas.ac.jp)

N. A. Tsyganenko, USRA, Code 695, Laboratory for Extraterrestrial Physics, NASA Goddard Space Flight Center, Greenbelt, MD 20771, USA. (Nikolai.Tsyganenko@gsfc.nasa.gov)